This is an open access article published under an ACS AuthorChoice License, which permits copying and redistribution of the article or any adaptations for non-commercial purposes.

NANO LETTERS

Letter

pubs.acs.org/NanoLett

Resonant Coupling between Molecular Vibrations and Localized Surface Plasmon Resonance of Faceted Metal Oxide Nanocrystals

Ankit Agrawal,[†] Ajay Singh,[†,‡] Sadegh Yazdi,[§] Amita Singh,[†] Gary K. Ong,[†,∥] Karen Bustillo,[‡] Robert W. Johns,[†,⊥] Emilie Ringe,[§,#] and Delia J. Milliron*[,†]

[†]McKetta Department of Chemical Engineering, The University of Texas at Austin, Austin, Texas 78712, United States

[‡]The Molecular Foundry and National Center for Electron Microscopy, Lawrence Berkeley National Laboratory, Berkeley, California 94720, United States

[§]Department of Materials Science and Nanoengineering, Rice University, 6100 Main Street, Houston, Texas 77005, United States

[∥]Department of Materials Science and Engineering, University of California, Berkeley, Berkeley, California 94720, United States

[⊥]Department of Chemistry, University of California, Berkeley, Berkeley, California 94720, United States

[#]Department of Chemistry, Rice University, 6100 Main Street, Houston, Texas 77005, United States

Supporting Information

ABSTRACT: Doped metal oxides are plasmonic materials that boast both synthetic and postsynthetic spectral tunability. They have already enabled promising smart window and optoelectronic technologies and have been proposed for use in surface enhanced infrared absorption spectroscopy (SEIRA) and sensing applications. Herein, we report the first step toward realization of the former utilizing cubic F and Sn codoped In_2O_3 nanocrystals (NCs) to couple to the C−H vibration of surface-bound oleate ligands. Electron energy loss spectroscopy is used to map the strong near-field enhancement around these NCs that enables localized surface plasmon resonance (LSPR) coupling between adjacent nanocrystals and LSPR-molecular vibration coupling. Fourier transform infrared spectroscopy measurements and finite element simulations are applied to observe and explain the nature of the coupling phenomena, specifically addressing coupling in mesoscale assembled films. The Fano line shape signatures of LSPR-coupled molecular vibrations are rationalized with two-port temporal coupled mode theory. With this combined theoretical and experimental approach, we describe the influence of coupling strength and relative detuning between the molecular vibration and LSPR on the enhancement factor and further explain the basis of the observed Fano line shape by deconvoluting the combined response of the LSPR and molecular vibration in transmission, absorption and reflection. This study therefore illustrates various factors involved in determining the LSPR−LSPR and LSPR−molecular vibration coupling for metal oxide materials and provides a fundamental basis for the design of sensing or SEIRA substrates.

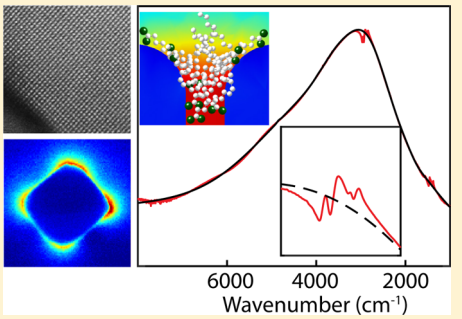

KEYWORDS: *Infrared plasmon, metal oxide, EELS, Fano resonance, SEIRA*

Plasmonic nanocrystals (NCs) are promising optical elements for a wide variety of applications owing to their ability to enhance and localize electric fields at an interface at the nanoscale, well below the diffraction limit.[1] This enhanced electric near field can couple to other optical transitions such as excitons, vibrations, and interband transitions to enhance the efficiency of various optical processes such as photoluminescence,[2,3] photon upconversion,[4−6] solar energy conversion,[7−9] and vibrational spectroscopy.[10−12] Specifically, coupling between localized surface plasmon resonances (LSPRs) and molecular vibrations can improve the sensitivity for detecting vibrational signatures, giving rise to techniques such as surface enhanced Raman spectroscopy (SERS)[11,12] and surface enhanced infrared absorption spectroscopy (SEIRA).[10,13] SERS has been extensively studied using Au[11,14] and Ag[15] NC LSPRs which conveniently appear in the visible spectral region. To demonstrate SEIRA, however, LSPRs must be located in the mid-IR which has been achieved primarily with micron-scale lithographically deposited Au,[16,17] Ag,[18] and recently Sn:In_2O_3[10] structures. Particularly, pioneering work of the latter on plasmonic metal oxide SEIRA[10] has already suggested that metal oxide systems can exhibit significantly less long-range coupling effects than classical metals, indicating that these materials can be organized or patterned at higher packing density to produce a higher spatial density of near-field hot spots.

To achieve a higher spatial density of hot spots, one approach is to utilize small colloidal NCs as has been demonstrated with Au nanoparticles for SERS applications.

Received: January 29, 2017
Revised: March 9, 2017

 © XXXX American Chemical Society

DOI: 10.1021/acs.nanolett.7b00404
Nano Lett. XXXX, XXX, XXX−XXX

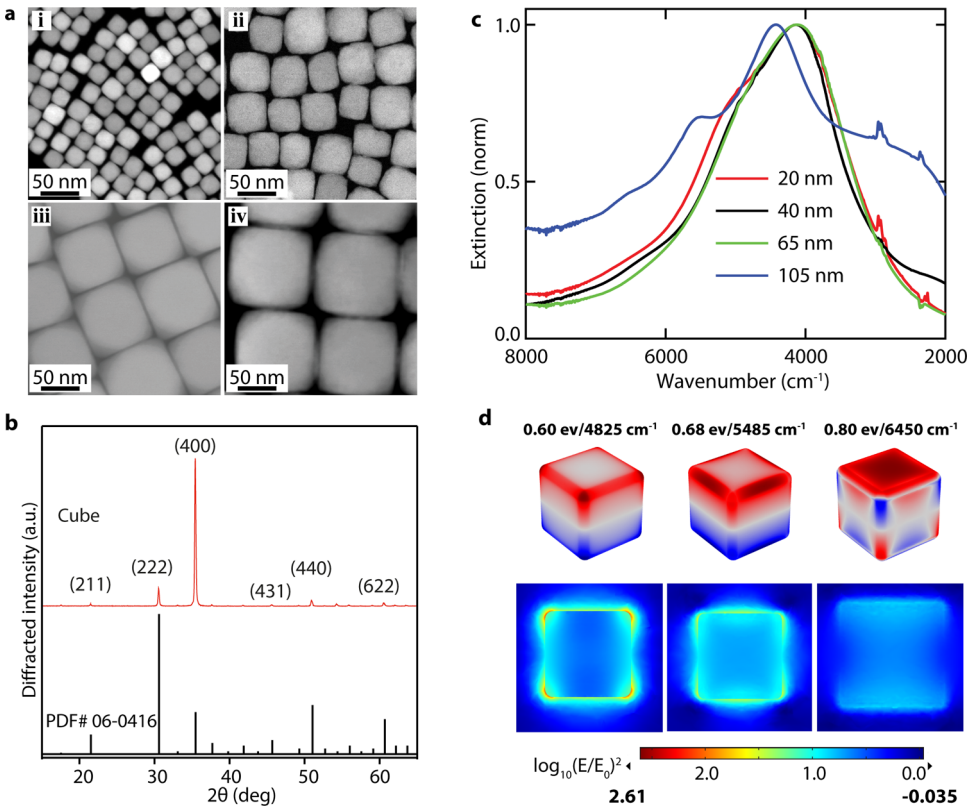

Figure 1. Characterization of FITO cubes. (a) STEM images of different sized cubic F, Sn-codoped In_2O_3 NCs with an average size (edge length) of (i) 20 nm, (ii) 40 nm, (iii) 65 nm, and (iv) 105 nm. (b) XRD pattern for 105 nm FITO cubes compared to the reference pattern for bixbyite In_2O_3. (c) Optical spectra of different sized cubic dispersed in TCE. (c, d) The fundamental modes are verified using optical simulation of an isolated FITO NC, which also suggests high NFE (shown on a $\log_{10}$ scale).

However, to access the mid-IR LSPR regime for SEIRA applications while preserving small NC sizes, we must consider plasmonic systems beyond that of Au and Ag. Recent developments in colloidal metal oxide NC synthesis and doping have introduced a library of plasmonic materials systems such as Sn:In_2O_3,[19−22] In:CdO,[23−25] Al:ZnO,[26,27] and so forth that exhibit LSPRs over the entire infrared region. These materials derive their plasmonic properties from degenerate doping and are therefore easily tuned to the desired resonance frequency (ω_{LSPR}) using ionizable defects such as oxygen vacancies and aliovalent dopants,[27−29] redox and photochemical charging,[30−32] or electrochemical modulation in NC films.[22,33−35] Furthermore, the optical properties of metal oxide NCs can be tuned separately from their morphology. This synthetic and postsynthetic tunability opens an opportunity to develop new high density, scalable, and *electrically tunable* or *chemically responsive* SEIRA substrates for application such as molecular sensing and catalysis. However, this is contingent upon first understanding the coupling behavior between molecular vibrations and metal oxide NC LSPRs. Such phenomena have yet to be reported and are studied here by a combined experimental and theoretical approach.

In general, coupled molecular vibration−LSPR systems can be modeled using a coupled harmonic oscillator system,[16,17,36−38] assuming the vibrational resonances behave as Lorentzian resonators. This approach, as applied to a lithographically defined gold model system,[16] has shown that the relative cross sections for scattering and absorption, and the relative resonance frequencies of the LSPR and vibrational resonances affects coupling between the two resonances and lead to different Fano lineshapes in the vibrational spectrum ranging from enhanced absorption, typical Fano derivative lineshapes or induced transparency However, for metal oxide systems, this response is expected to differ owing to plasmonic metal oxides being low loss materials that are semitransparent in the IR. Furthermore, in the case of NC films, the interplay of size, shape, and arrangement in determining all of the aforementioned optical parameters must be addressed.

Coupling to vibrational modes is enabled by the concentration of IR light around a plasmonic nanostructure when molecules with resonant modes are present in the adjacent space. Qualitatively, the strength of light concentration adjacent to plasmonic nanostructures, or near field enhancement (NFE), depends upon many factors including carrier concentration,[25] electron scattering,[25,39−42] and corner sharpness[10,25,29,39] (shape). Even higher NFE can be obtained by coupling plasmonic nanostructures in narrow gaps between structures where these "hot spots" can exhibit at least an order of magnitude stronger electric fields compared to those surrounding isolated nanostructures.[43−45] Summarizing our current knowledge of how NFE could manifest in plasmonic metal oxide NC systems, we expect maximum NFE for systems with a high carrier concentration but low carrier scattering combined with a shape with sharp edges, preferably assembled into an extended array, creating inter-NC hot spots. Having outlined these considerations, we synthesized cubic codoped Sn,F:In_2O_3 as an ideal model system to study the coupling behavior between a metal oxide NC LSPR and molecular vibrations, specifically the C−H vibrations of native oleate ligands.

DOI: 10.1021/acs.nanolett.7b00404
Nano Lett. XXXX, XXX, XXX−XXX

In this work, we demonstrate that the NFE around doped indium oxide NCs is substantial and it facilitates coupling between NCs in self-assembled arrays and further between NC LSPRs and molecular vibrations. Specifically, we share the synthetic protocol for variable-sized colloidal cubes of fluorine (F) and tin (Sn) codoped In_2O_3 (FITO) and characterize the presence and influence of the near field around these highly faceted NCs. Incorporation of F^- dopant into $Sn:In_2O_3$ was found to yield more cubic NCs and decrease electron scattering, which improves the quality factor of the LSPR compared to $Sn:In_2O_3$. We report the size-dependent LSPR spectra of FITO, map the NFE around a single cubic NC via scanning transmission electron microscopy-electron energy loss spectroscopy (STEM-EELS), and compare these results with far-field and near-field electromagnetic simulations. Interactions between LSPR modes of adjacent NCs in a chain and in a 2×2 array give rise to coupled modes that are mapped via EELS. Molecular vibrations, specifically C−H stretching modes of the surface-bound ligands, are shown to couple to the coupled LSPR modes in NC arrays. The dependence of coupling on the carrier concentration and NC size is apparent in systematic changes in the Fano line shape observed by Fourier transform infrared spectroscopy (FTIR). The interpretation of these results is bolstered by modeling and electromagnetic simulations that enables us to delineate the convoluted dependence of Fano line shape on several parameters such as size of the NC, coupling strength, and LSPR frequency. For this purpose, temporal coupled mode theory (TCMT) was developed in this work as applied to a coupled system of metal oxide LSPRs and multiple molecular vibrational modes.

Results and Discussion. Doped In_2O_3 NCs were synthesized using standard Schlenk line air-free colloidal synthesis techniques with a synthetic protocol based upon the decomposition of a metal oleate at high temperatures in an organic solvent and in the presence of mixed primary and tertiary amine to yield the metal oxide [see Section S1 in Supporting Information (SI) for more details]. In Figure 1a, scanning transmission electron microscopy (STEM) analyses of different sizes of doped In_2O_3 NCs are shown, illustrating the tight control on size (edge length) of the cubic FITO (Figure 1a, low-magnification images for all sizes, and high-resolution images for the 40 nm cubes are in Figure S1). The average size (20−120 nm) of the NCs can be tuned by varying the ratio of primary and tertiary amines and the growth time (see SI for details). X-ray diffraction (XRD) shows (Figure 1b) that FITO NCs possess the cubic bixbyite structure typical of In_2O_3, with a strong (100) texture arising from preferential orientation of nanocubes with their square faces lying flat on the substrate.

The optical extinction spectra of the four representative samples as colloidal dispersions do not vary significantly with the size of the NCs (Figure 1c) because the NCs are isolated from one another. Note that the secondary peak at lower energy for the 105 nm sample is due to coupling between NCs as a result of slight NC aggregation in tetrachloroethylene (TCE). These NCs are all sufficiently small that we expect the electric field inside the NCs to be largely size invariant per the quasi-static approximation[46] that is valid for particle sizes well below the excitation wavelength (here, approximately 2500 nm). In electromagnetic simulations of the optical response (Figures S2 and S3), we found that, in this size regime, absorption is dominant and size-independent, while scattering contributes little to the extinction spectra. However, the NC size was found to strongly influence coupling, as discussed below.

Dopant type and distribution inside each NC can significantly impact LSPR spectra and near-field properties. In the case of $Sn:In_2O_3$, carrier mobility and hence LSPR damping are substantially influenced by ionized impurity scattering at dopant sites and oxygen vacancy defects ($Sn_{In}^{\bullet}$ and $C_O^{\bullet\bullet}$ in Kröger−Vink notation). It was recently shown that defect engineering by doping In_2O_3 NCs with cerium can greatly reduce dopant related ionized impurity scattering, but the achievable carrier concentrations were much lower than those attainable with tin doping.[39] Here, we have instead incorporated fluorine as a codopant with tin in the In_2O_3 NCs. Fluorine ions likely occupy oxygen sites ($F_O^{\bullet}$), contribute free electrons, and can decrease the oxygen vacancy concentration. Since the cross section for ionized impurity scattering is proportional to the square of ionic charge (Z^2), $F_O^{\bullet}$ defects will scatter electrons more weakly than oxygen vacancies ($V_O^{\bullet\bullet}$) with the overall effect being that fluorine codoping can reduce LSPR damping while maintaining a high carrier concentration. To understand the effect of fluorine incorporation on far field optical properties, the full-width at half-maximum (fwhm) of the LSPR was used to quantify damping. We compared the simulated extinction spectrum of FITO cubes (Figure S4), with that of $Sn:In_2O_3$ (ITO) cubes, using the same geometry for each (Figure S2) to isolate the impact of differences in scattering. The dielectric function of ITO was taken from previously published work,[47] while the FITO dielectric function was determined by fitting spectra of the 20 nm cubes reported here (see SI). The reduction of damping upon incorporation of fluorine is apparent in the narrower LSPR peak of the FITO cubes, as expected. The reduction of ionized impurity scattering in FITO also suggests that higher NFE may be achievable under resonant excitation of these NCs.

The optical spectra and near field map (Figure 1c and d) reflect the convolution of three fundamental geometric eigenmodes, i.e., corner, edge, and face-centered modes from low to higher energy, respectively. Simulated surface charge maps of a 20 nm FITO NC under excitation at different energies (Figure 1d, top, 100 nm cube reported in Figure S5) show that all of the geometrical modes are of dipolar nature (details of the modeling are reported in Section S2 of the SI). The NFE maps (Figure 1d, bottom) show that the sharp edges and reduced ionized impurity scattering in FITO results into larger NFE (>400) than previously reported values for spherical (∼10)[6] and rod-like ITO (150−160).[10]

To observe the expected LSPR modes experimentally, we mapped the plasmon-induced near field properties of FITO cubes with high spatial resolution using monochromated STEM-EELS (zero-loss peak fwhm of 0.15 eV), performed in an FEI Titan Themis[3] equipped with a Gatan Quantum ERS electron spectrometer. To extract the LSPRs' spatial and spectral distribution, the global fitting technique of non-negative matrix factorization (NMF)[48−54] was applied to the recorded spectrum images (Section S4 in SI and Figures S7−S8). Figure 2a shows the three distinct LSPR modes at (0.62 eV/5000 cm^{-1}, 0.73 eV/5888 cm^{-1}, 0.85 eV/6855 cm^{-1}) of a single FITO cube on a 10 nm thick SiN substrate. Even though the excitation mechanism in experimental EELS and optical simulation are different (electrons and photons, respectively), the plasmon peak energies in the EEL spectra are similar to that obtained via experimental FTIR and simulated spectra. The EEL spectra thereby verify the presence of different geometric

DOI: 10.1021/acs.nanolett.7b00404
Nano Lett. XXXX, XXX, XXX−XXX

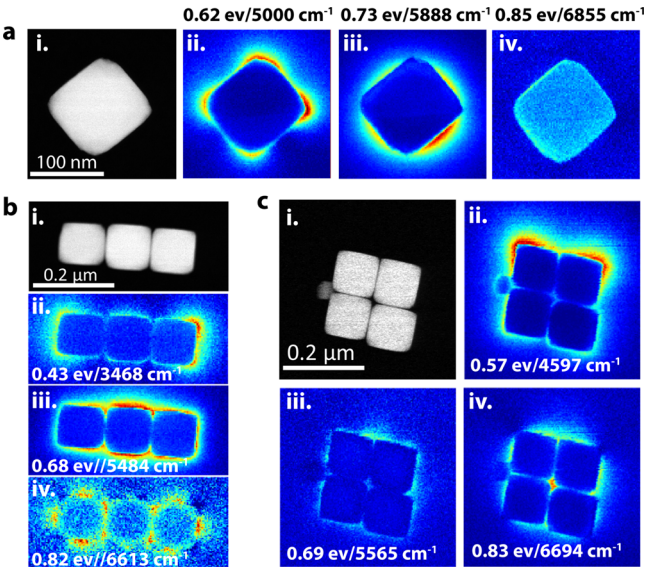

Figure 2. STEM-EELS plasmon maps. Spatial distribution of localized surface plasmon modes extracted, using non-negative matrix factorization (NMF) method, from spectrum images acquired by STEM-EELS for (a) a single FITO NC, (b) 1D chain of three FITO nanocubes, and (c) 2D array of 2 × 2 FITO nanocubes. For the single cube, EELS plasmon maps show the corner, edge, and face geometrical eigenmodes at 0.62, 0.73, and 0.85 eV, respectively. For the 1D chain and 2D array, the LSPR peaks shift, and extra modes appear due to coupling (spectra are shown in Figure S9).

modes (Figure 2a) in metal oxide NCs, in good agreement with the simulated near field map (Figure 1d). In agreement with current and previous simulations,[49] these EELS maps are the first direct evidence establishing that plasmonic metal oxide NCs exhibit near-field modes similar to those in faceted gold and silver nanoparticles that have been the key to developing numerous applications of plasmonic materials.

Assembling NCs into extended structures leads to LSPR modes arising from NC−NC coupling that causes both more intense and a higher density of near field hotspots.[43,55,56] Recently, Kuznetsov[57] demonstrated computationally that although individual metal oxide NCs have weaker NFE than metal nanoparticles, coupled metal oxide structures have higher volumetrically average NFE than similar metallic nanostructures due to their higher spatial hot spot density. We examined the LSPR coupling of FITO NCs, first by mapping the LSPR modes of small NC clusters on SiN substrates and then by extending our study to mesoscale film of self-assembled NCs. The LSPR modes of both a linear chain of three NCs and a 2 × 2 square array of NC cubes were observed by EELS (Figure 2b,c and Figures S9−12). In both cases, the lowest energy modes spanned the cluster as a single entity and shifted toward lower energy compared to isolated NC due to strong LSPR−LSPR coupling (Figure 2b-ii and 2c-ii). For instance, in the linear structure, the modes at 0.43 ev/3468 cm^{-1} and 0.68 eV/5484 cm^{-1}, respectively, are localized at the geometrical corners and edges of the overall chain structure. Similarly, for the 2 × 2 structure, the mode at 0.57 eV/4597 cm^{-1} is localized at the corners of the overall structure. Prior literature[49,53,58] on plasmon coupling in clusters of Au nanoparticles has shown that, for closely spaced particles, clusters of NCs behave as a single entity with LSPR modes that extend across the overall structure. Since our system of 105 nm cubes had an average 3 nm face to face separation due to surface bound ligands, which is very small compared to the size of the NC, our observation appears consistent with this expectation. However, alongside the expected assembly spanning modes, we also observed localized internal modes such as one at 0.8 eV, which produces a hot spot localized at the center of the (2 × 2) array. Overall, the EELS maps of these NC clusters prove that coupled and individual metal oxide NCs support the formation of LSPR modes and hot spots, just as for noble metals, so these materials offer a new alternative for applications based on near-field enhancement of infrared light.

For SEIRA in particular, maximizing the effective optical density of a molecular vibration is desired, and this is best achieved by assembling NCs over a large substrate area to create a high density of hot spots with strong NFE. Extended close-packed assemblies of FITO cubes were prepared by drop casting NC solutions on a CaF_2 substrates and drying slowly to yield close-packed layers (Figure 3a). The optical response of extended arrays of FITO cubes was simulated for each sample size and then compared to the experimental spectra. The simulation employs periodic boundary conditions in two dimensions for a monolayer of NCs on a CaF_2 substrate to approximate the experimental conditions (Section S5 in SI and Figure S13). Spectra were calculated using the COMSOL wave optics module while varying the size of the NCs keeping the interparticle distance constant. As the ratio ($R = d/a$) between interparticle distance (d) and NC size (a) decreases, coupling between the LSPR of neighboring NCs becomes stronger, resulting in a redshift of the LSPR in the extinction spectrum toward lower energy (Figure 3b). In the experimental extinction spectra, a similar trend is observed as NC size increases (Figure S14). This result demonstrates that in contrast to size independent optical extinction in solution where the interparticle coupling is very weak; in assembled films, the size of the NCs governs the extent of LSPR−LSPR coupling. Moreover, at first look, the decrease in transmittance for larger NCs could be rationalized by an increase in the amount of material in a NC monolayer. However, a closer view of the simulation results shows that losses due to both reflection and absorption contribute to this change in the extinction (Figure 3c). As R decreases, the effective refractive index approaches that of continuous TCO film, and the larger NC films are substantially reflective. In the simulated spectra, the LSPR absorbance and reflectance redshift as R decreases, while the reflectance monotonically increases in intensity (Figure S15). The absorption is predicted to peak at around 40% of the incident light for 40 nm NC (Figure S15).

Simulations of the NFE of infrared light at the energy where extinction is strongest show that the strongest enhancement is in hot spots between assembled NCs (Figure 3d). As R decreases, the NFE increases (Figure 3e, black). The influence of NC size on LSPR−LSPR coupling in films is an increase in reflection intensity compared to absorption intensity at larger sizes and increased near field coupling as NC size increases (Figure 3e). Next, we will examine the influence of both of these factors on coupling between the LSPR of assembled NC films and the vibrational resonance of C−H bonds in adsorbed molecules.

Coupling between relatively broad plasmonic resonances and sharp vibrational resonances of molecular bonds can result in Fano-type interference ranging from plasmon-induced transparency to plasmon-enhanced absorption.[16,36,37] Such resonant coupling effects have been studied using 2D-graphene structures,[59] gold nanorods,[16] and other metallic structures[60,61]

DOI: 10.1021/acs.nanolett.7b00404
Nano Lett. XXXX, XXX, XXX−XXX

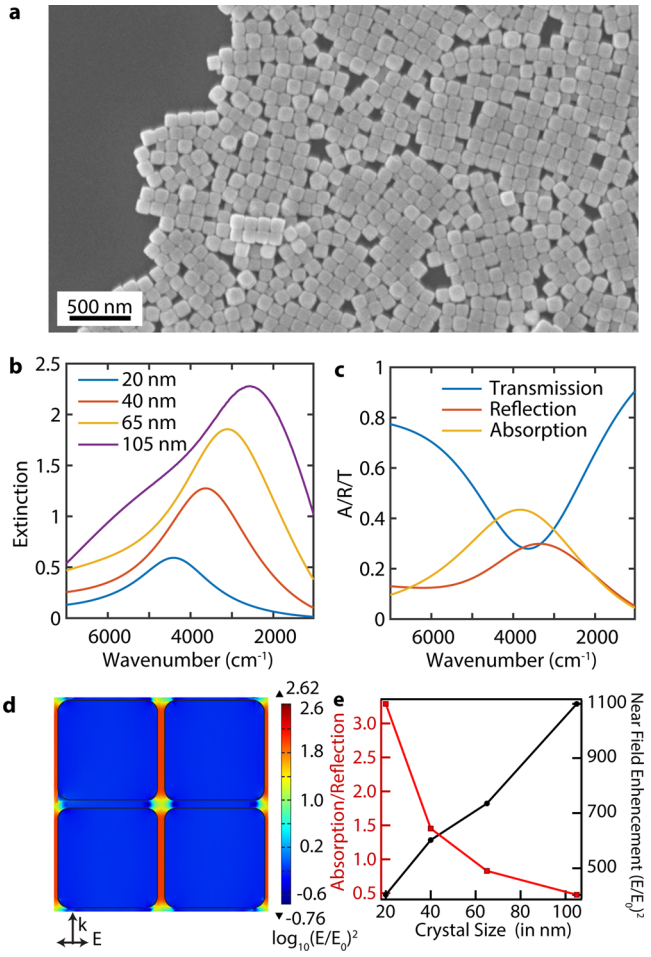

Figure 3. Optical properties of coupled NC assemblies. (a) Scanning electron microscopy (SEM) image of a slowly dried drop cast film of 105 nm FITO NCs. (b) Simulated extinction spectra of periodic monolayer film of closed packed FITO NCs of different sizes. The distance (d) between the NCs was kept fixed while changing their size (a). As the size increases, the ratio $R = d/a$ decreases, resulting in stronger LSPR−LSPR coupling; increased coupling shifts the LSPR toward lower energy. (c) Simulated reflection, transmission, and absorption spectra of a 40 nm NC assembly. (d) Simulated NFE map at the extinction peak for a 105 nm NC assembly with light polarized laterally. The formation of hot spots in between the NCs leads to an order of magnitude increase in NFE compared to an isolated NC. (e) The ratio of absorption to reflection decreases (red line) and maximum NFE increases (black line) with the increasing size.

with infrared resonances. In most of these previous studies, a reflective gold substrate is used, and spectra are collected in reflection geometry. For the plasmonic system consisting of gold nanorods separated from a gold substrate by a thin layer of PMMA, Altug et al.[16] observed that, if the LSPR frequency is resonant with the molecular vibration frequency, the coupling behavior between them qualitatively changes depending upon the ratio of plasmon decay rate to scattering and absorption. If this ratio is less than 1, coupling gives rise to plasmon-induced transparency of the vibrational signal and if it is greater than 1, enhanced absorption is observed. In related works, Altug et al.[36,37] and Shvet et al.[17] have shown that off resonant coupling results in a Fano-like derivative line shape. All of these observations can be rationalized using coupled harmonic oscillators as a model of TCMT[16,17,62] (Figure 4a,b).

Here, we have studied the coupling between semitransparent (in the IR spectral range) films of FITO NCs on CaF_2 substrates and different C−H stretching modes of NC-bound oleate molecules, which are sharp resonances in the range of (2800−3100 cm^{-1}, Figure S7). Oleic acid is bound to the NC surfaces during colloidal synthesis, and a monolayer remains adsorbed following isolation of the NCs, which allows us to prepare thin films from solvent dispersions. FTIR transmission spectra are recorded at a perpendicular angle of incidence relative to the substrate and reported as extinction (Figure 4c). The oleic acid vibrational signature is observed on top of an intense LSPR signal (Figure 4c, inset). To isolate the vibration signal and investigate coupling between the resonators, the transmittance was divided by a polynomial fit to the plasmon line shape (Figure 4c, red). The derivative shape of the vibrational signal is Fano-like and indicative of coupling. Hence, we anticipate dependence of this line shape on two main parameters, namely, the NC size and the detuning of the LSPR frequency with respect to the vibrational resonance ($\Delta\omega = \omega_{LSPR} - \omega_{vib,avg}$).

To examine the spectral changes induced by detuning, we varied the LSPR frequency by synthetically changing the tin dopant concentration in 20 nm NCs. As the free electron concentration increases with doping, the LSPR peak shifts from lower to higher energy relative to the vibrational resonance (Figure S16 and Figure 4d). For the lowest energy LSPR, each vibrational band appears as a dip in extinction, indicating plasmon-induced transparency, while for higher energy LSPR the asymmetric Fano-like line shape appears. This indicates that, indeed, the FITO LSPR is coupling to the oleic acid molecular vibrations. We compare this trend to numerical simulations of the coupled optical response (Figure S16 and Figure 4d). In the numerical simulation, a two-dimensional periodic structure consisting of a monolayer of ligand coated 20 nm NCs was excited at normal incidence. The simulated extinction spectra were background subtracted in the same way as the experimental spectra to obtain the vibration signature. The LSPRs in the simulations were chosen to match the range of experimental detuning. The simulated spectral profiles matched the experimental results, although the strength of the vibrational signals seems to be overestimated by the simulations, which will be discussed below. The variations in vibrational lineshapes resulting from LSPR−vibrational coupling are attributed to changes in frequency detuning since we do not expect substantial differences in NFE or relative value of reflection to absorption over this narrow energy range.

We expect the NC size to alter the observed vibrational line shape owing to its influence on far field reflection, transmission, and absorption in organized NC films. As observed, the vibrational signal has a Fano-like line shape for a film of 20 nm NCs, which evolves toward plasmon-induced transparency for 40, 65, and 105 nm NCs due to a progressive red shift of the plasmon resonance from positive to negative detuning with increasing size, due to stronger LSPR−LSPR coupling of larger NCs (Figure S17, Figure 4e). These trends are counterintuitive relative to the understanding outlined in literature regarding LSPR in conventional metal nanostructures. From prior literature on coupling in classical metal plasmonic systems,[16,36] we expect a recovery of an asymmetric Fano line shape once the LSPR frequency is red-shifted away from the molecular vibration, such as the case of 65 and 100 nm NC films. Indeed, as explained earlier, the derivative-like Fano line shape did appear when we detuned the LSPR by varying

DOI: 10.1021/acs.nanolett.7b00404
Nano Lett. XXXX, XXX, XXX−XXX

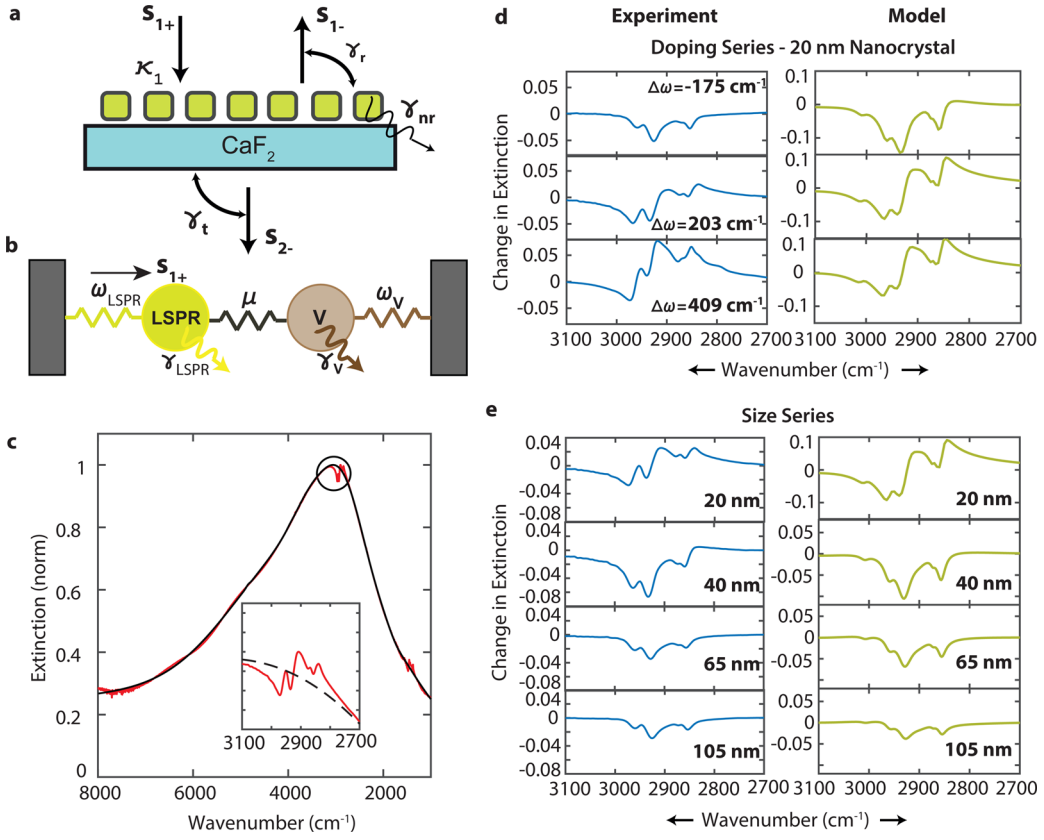

Figure 4. Plasmon−vibrational mode coupling: (a) Schematic depicting the interaction between the incident light (s_{1+}) and periodic film of cubic NCs with the coupling constant (κ_1). Plasmon excitation decays through both radiative and nonradiative pathways. It couples with reflected and transmitted light at plasmon decay rate γ_r and γ_t, respectively. The nonradiative decay rate (γ_{nr}) determines the absorption in the film. (b) Schematic illustrating the coupling between LSPR and vibrational resonance, describing both as harmonic oscillators. (c) Measured extinction spectrum of a film of 20 nm ligand capped NCs. Inset: Zoom-in on the coupling zone showing the Fano resonant coupling signature. (d) Left panel—background subtracted vibrational signal changes from plasmon induced transparency to Fano interference with increase in detuning between the LSPR and the vibrational resonances. The NCs were 20 nm in all cases. Right panel—the simulation of transmittance for periodic structures of ligand bound NCs reproduces the same coupling behavior as observed in experimental spectra. (e) Left panel—coupling between different sized NCs in a film with vibrational resonance changes from Fano resonance for 20 nm to plasmon-induced transparency for larger sizes. Right panel—the simulation of transmittance for periodic structures of ligand-bounded NCs of different size with fixed interparticle distance reproduces the observed behavior.

doping (at constant 20 nm size). This contrast between the size dependence and dopant dependence on the line shape suggests that some other size-dependent properties of the NCs, rather than only detuning are responsible for the persistence of the plasmon-induced transparency in the self-assembled films of larger NCs. A closer analysis utilizing numerical simulation is required to explain the trends and is discussed below.

Energy stored in a resonant process like an LSPR gets dissipated to its surrounding via both radiative and nonradiative processes. Here, in the case of a periodic film, the available nonradiative channel would be absorption, and the radiative channels would include both reflection and transmission. In a coupled resonance system, coupling would be exhibited differently in each decay channel. As expected, simulations show that the signatures of coupling in absorption, reflection and transmission differ from each other and depend strongly on the size of the NCs (Figure S18). Background subtracted molecular vibration spectra (Figure S19) show that, with increasing NC size, the coupling profile in absorption spectra changes from asymmetric Fano-like resonance (20 nm) to a complete induced transparency (40 nm) and then to enhanced absorption (65 and 105 nm). In contrast, the reflection spectra always show a plasmon-induced transparency irrespective of NC size. So, as the relative contributions of reflection and absorption to the measured transmittance spectra change with NC size, the line shape changes from asymmetric (20 and 40 nm) to a plasmon-induced transparency (65 and 100 nm). For 20 nm NC films (for all dopant concentrations), where absorption is dominant over reflection, the absorption spectrum determines the shape of the vibrational resonances in extinction spectra. At the other size extreme, in a 100 nm NC film, it is the vibrational signature in reflection that is dominant in the extinction spectrum. Simulated near-field maps also show that, even though there is higher NFE at the peak LSPR energy with increasing size, the NFE decreases at the actual vibration frequency (2850 cm^{-1}) (Figure S20) because the detuning between the LSPR and vibration increases as the larger NCs couple more to each other. This trend explains our observation of a decrease in vibrational signal strength with increasing NC size. That said, the trends in vibrational line shape observed here differ from those in the literature on classical metal systems. To understand this behavior in greater depth, taking inspiration from the works of Altug et al.,[16] Haus et al.,[63] and Fan et al.,[62,64] we developed a theoretical model to further explain our results.

TCMT analysis used previously to rationalize coupling effects in plasmonic systems based on classical metals cannot be directly applied as it assumes only one optical port with

DOI: 10.1021/acs.nanolett.7b00404
Nano Lett. XXXX, XXX, XXX−XXX

incident and reflected light (Section S6 in SI). For semitransparent (in the IR range) metal oxide films, we need to consider all three components of electromagnetic waves, that is, reflected, transmitted, and absorbed light. With this consideration, we developed a theoretical model to explain the optical properties using two port coupled mode theory.

As shown schematically in Figure 4a, the plasmonic resonators are coupled to incident (s_{1+}) and reflected (s_{1-}) light through port 1, and transmitted light (s_{2-}) through port 2, where the ± sign signifies an incoming or outgoing wave. LSPR and vibrational resonators are modeled as simple harmonic oscillators. Energy exchange between these resonators occurs due to interaction between the LSPR-induced near field and the vibrational oscillators with a magnitude determined by the coupling rate, μ. This coupled harmonic oscillator system is represented as,

$$\frac{\mathrm{d}}{\mathrm{d}t}\phi(t) = [j\omega_{\mathrm{LSPR}} - (\gamma_{\mathrm{r}} + \gamma_{\mathrm{t}} + \gamma_{\mathrm{nr}})]\phi(t) + \kappa_1 s_{1+} + j\sum \mu_i P_i \tag{1}$$

$$\frac{\mathrm{d}}{\mathrm{d}t}P_i(t) = [j\omega_v^i - \gamma_v^i]P_i(t) + j\mu_i\phi(t) \tag{2}$$

where, in eq 1, $|\phi(t)|^2$ is the energy stored in LSPR resonator, ω_{LSPR} is LSPR frequency of the resonator, γ_{r} is the energy loss rate in reflection, γ_{t} is the energy loss rate in transmission, γ_{nr} is nonradiative energy loss rate, κ_1 is the coupling coefficient to incoming light s_{1+}, and μ_i is the coupling coefficient to ith vibration resonance, P_i. In eq 2, $|P_i(t)|^2$ is the energy stored in the ith vibration resonance, ω_v^i and γ_v^i are the central frequency and line width of ith vibrational resonance, respectively.

The energy balance between incoming and outgoing waves is represented by,

$$s_- = Cs_+ + K\phi(t) \tag{3}$$

where C is the nonresonant scattering matrix and K is $[(2\gamma_{\mathrm{r}})^{1/2}(2\gamma_{\mathrm{t}})^{1/2}]^T$.

These equations can then be simplified (for the detailed mathematical derivation, see section S6 in SI) to derive transmission and reflection intensity as,

$$T(\omega) = \left| t_{\mathrm{D}} - \left\{ \frac{\sqrt{4\gamma_{\mathrm{r}}\gamma_{\mathrm{t}}}}{j(\omega - \omega_{\mathrm{LSPR}} - \sum \omega_\mu^i) - (\gamma_{\mathrm{tot}} + \sum \gamma_\mu^i)} e^{j\theta} \right\} \right|^2 \tag{4}$$

$$R(\omega) = \left| r_1 - \left\{ \frac{2\gamma_{\mathrm{r}}}{j(\omega - \omega_{\mathrm{LSPR}} - \sum \omega_\mu^i) - (\gamma_{\mathrm{tot}} + \sum \gamma_\mu^i)} e^{j\theta_1} \right\} \right|^2 \tag{5}$$

where t_{D} and r_1 are nonresonant transmission and reflection, γ_{tot} is the net plasmon loss which equals $\gamma_{\mathrm{r}} + \gamma_{\mathrm{t}} + \gamma_{\mathrm{nr}}$, θ is the transmission phase, θ_1 is the reflection phase, and γ_μ^i and ω_μ^i expressed as

$$\omega_\mu^i = \frac{\mu^2(\omega - \omega_v^i)}{[(\omega - \omega_v^i)^2 + (\gamma_v^i)^2]} \tag{6}$$

$$\gamma_\mu^i = \frac{\mu^2\gamma_v^i}{[(\omega - \omega_v^i)^2 + (\gamma_v^i)^2]} \tag{7}$$

Applying TCMT (eqs 4 and 5, and Figure S21), the lineshapes of the vibrational signal in reflection, transmission, and absorption spectra agree between our experimental and modeling results. Derived reflection and transmission equations (eqs 4 and 5) were used to deconvolute the effect of various contributing factors such as plasmon resonance energy decay rates in reflection (γ_{r}), transmission (γ_{t}), and absorption (γ_{nr}) as well as LSPR frequency and coupling constant (μ), in determining the line shape of the coupled vibrational signals. The sensitivity of the coupled vibrational signal line shape to each of the factors was determined by changing one parameter at a time while keeping all others fixed. Our results show that, as we increase γ_v, the coupled vibration signal intensity increases with no change in the line shape of either the reflection or transmission spectrum (Figure S22). The similar behavior was observed when only ω_{LSPR} (Figure S23) or μ (Figure S24) were changed. These trends suggest that the change in vibrational line shape with increasing NC size is due to the synergistic effects of simultaneous changes in decay rates (γ_{r}, γ_{a}, and γ_{t}). To verify this hypothesis, the impact of simultaneous changes in relative decay rates $\gamma_{\mathrm{r}}/\gamma_{\mathrm{t}}$ and $\gamma_{\mathrm{a}}/\gamma_{\mathrm{t}}$ while keeping other parameters such as ω_{LSPR} and NFE fixed was examined. This prediction was done for 20 and 65 nm NC films, where the differences in decay rates were maximized. The results of this theoretical prediction reproduced the similar coupling lineshapes as observed in experiments with some difference in signal intensity (Figure S25). This conclusively shows that the vibrational lineshapes are governed by the plasmon decay dynamics. The relative decay rates $\gamma_{\mathrm{r}}/\gamma_{\mathrm{t}}$ and $\gamma_{\mathrm{a}}/\gamma_{\mathrm{t}}$ determine the Fano lineshapes of coupled vibrational−LSPR spectra, and the vibrational signal intensity is determined by several factors such as ω_{LSPR}, NFE, and ligand volume fraction. Our experimental observations, unraveled by both simulations and TCMT, indicate that for semitransparent metal oxide NC films, coupling between the LSPR and molecular vibrations depends not only on the NFE; it also depends on the relative far field resonance decay rates in reflection, transmission, and absorption spectrum. For applications such as SEIRA, sensing, or catalysis, where it is crucial to maximize the interaction between the LSPR and the vibrational resonance, thinking of the system as a whole is crucial. Not only do the NC properties matter, but how they are arranged also impacts the coupling interactions achievable in the system. Since the size and shape impact self-assembly in NC systems, changing one must account for how they impact the final coupled NC spectral properties, which can be strongly dependent on the assembled mesoscale structure.

In conclusion, we discerned the nature of coupling between molecular vibrational modes of the native ligands and metal oxide plasmonic NCs. This was achieved by using colloidially synthesized F−Sn codoped In_2O_3 cubic NCs of variable size (20−110 nm), which enabled efficient localization of electric fields around the NCs due to low ionized impurity scattering. This study highlights that an innovative synthetic strategy such as codoping can substantially improve the quality factor of metal oxide NCs, providing a favorable alternative to metallic systems. Using EELS, we experimentally mapped the fundamental geometrical LSPR modes in single NCs as well as in small NC clusters, which were previously hypothesized to

DOI: 10.1021/acs.nanolett.7b00404
Nano Lett. XXXX, XXX, XXX−XXX

exist in computational studies. Exploiting the promising NFE properties, these materials were employed to demonstrate and understand the nature of plasmon−molecular vibration coupling for metal oxide systems. Specifically, we investigated the coupling between C−H stretches of native oleate ligands and NC films and showed that the Fano line shape is highly dependent upon the optical decay rates of available pathways, i.e., reflection, transmission, and absorption. This finding is contrary to the popular belief that NFE and optical detuning are the sole factors governing the coupling signature of the interaction between an LSPR and molecular vibrations. Furthermore, the computational model and theoretical TCMT as applied to metal oxide systems developed in this work could be easily extended to other material systems and will facilitate the study of metal oxides in greater depth. Although this study showcases the promise of metal oxide systems for coupling applications, it does not take into account the potential effects of dopant distribution, dopant activation, and molecular vibration orientation relative to the NC surface on the coupling between NC LSPR and molecular vibrations. However, future studies addressing the aforementioned effects will be improvements upon the foundational work presented here that may already be of relevance to potential applications ranging from catalysis, SEIRA, and integrated optoelectronics. We hope that this study will motivate researchers to investigate metal oxide systems toward developing electrically or photo-(chemically) tunable substrates for various mid-IR optical applications.

■ ASSOCIATED CONTENT

Supporting Information

The Supporting Information is available free of charge on the ACS Publications website at DOI: 10.1021/acs.nanolett.7b00404.

Additional information on synthesis, single nanocrystal modeling, electron energy loss spectroscopy, periodic boundary simulations, and temporal coupled mode theory (PDF)

■ AUTHOR INFORMATION

Corresponding Author

*E-mail: milliron@che.utexas.edu.

ORCID

Ankit Agrawal: 0000-0001-7311-7873

Delia J. Milliron: 0000-0002-8737-451X

Author Contributions

Ankit Agrawal and Ajay Singh contributed equally to this work.

Notes

The authors declare no competing financial interest.

■ ACKNOWLEDGMENTS

This work was performed at the University of Texas at Austin and Rice University in Houston. A.A., A.S., A.S., G.K.O., R.W.J., and D.J.M. acknowledge the funding from the Welch Foundation (F-1848) and the National Science Foundation (CHE-1609656). EELS results were obtained at the Electron Microscopy Center (EMC) of Rice University. High and low resolution ADF-STEM images were obtained at National Center for Electron Microscopy (NCEM), Lawrence Berkeley National Laboratory, a user facility supported by the Office of Science, Office of Basic Energy Sciences, of the U.S. Department of Energy under contract no. DE-AC02-05CH11231.

■ REFERENCES

(1) Agrawal, A.; Johns, R. W.; Milliron, D. Control of Localized Surface Plasmon Resonances in Metal Oxide Nanocrystals. *Annu. Rev. Mater. Res.* **2017**, DOI: 10.1146/annurev-matsci-070616-124259.

(2) Akselrod, G. M.; Weidman, M. C.; Li, Y.; Argyropoulos, C.; Tisdale, W. A.; Mikkelsen, M. H. Efficient Nanosecond Photoluminescence from Infrared PbS Quantum Dots Coupled to Plasmonic Nanoantennas. *ACS Photonics* **2016**, *3* (10), 1741−1746.

(3) Hoang, T. B.; Akselrod, G. M.; Argyropoulos, C.; Huang, J.; Smith, D. R.; Mikkelsen, M. H. Ultrafast Spontaneous Emission Source Using Plasmonic Nanoantennas. *Nat. Commun.* **2015**, *6*, 7788.

(4) Lu, D.; Mao, C.; Cho, S. K.; Ahn, S.; Park, W. Experimental Demonstration of Plasmon Enhanced Energy Transfer Rate in $NaYF_4$:Yb^{3+},Er^{3+} Upconversion Nanoparticles. *Sci. Rep.* **2016**, *6*, 18894.

(5) Yin, Z.; Zhou, D.; Xu, W.; Cui, S.; Chen, X.; Wang, H.; Xu, S.; Song, H. Plasmon-Enhanced Upconversion Luminescence on Vertically Aligned Gold Nanorod Monolayer Supercrystals. *ACS Appl. Mater. Interfaces* **2016**, *8* (18), 11667−11674.

(6) Furube, A.; Yoshinaga, T.; Kanehara, M.; Eguchi, M.; Teranishi, T. Electric-Field Enhancement Inducing Near-Infrared Two-Photon Absorption in an Indium−Tin Oxide Nanoparticle Film. *Angew. Chem., Int. Ed.* **2012**, *51* (11), 2640−2642.

(7) Catchpole, K. R.; Polman, A. Design Principles for Particle Plasmon Enhanced Solar Cells. *Appl. Phys. Lett.* **2008**, *93* (19), 191113.

(8) Yu, Z.; Raman, A.; Fan, S. Fundamental Limit of Nanophotonic Light Trapping in Solar Cells. *Proc. Natl. Acad. Sci. U. S. A.* **2010**, *107* (41), 17491−17496.

(9) Gan, Q.; Bartoli, F.; Kafafi, Z. Plasmonic Nanostructures Improve Solar Cell Performance. *SPIE Newsroom* **2013**, DOI: 10.1117/2.1201308.005013.

(10) Abb, M.; Wang, Y.; Papasimakis, N.; de Groot, C. H.; Muskens, O. L. Surface-Enhanced Infrared Spectroscopy Using Metal Oxide Plasmonic Antenna Arrays. *Nano Lett.* **2014**, *14* (1), 346−352.

(11) Stiles, P. L.; Dieringer, J. A.; Shah, N. C.; Van Duyne, R. P. Surface-Enhanced Raman Spectroscopy. *Annu. Rev. Anal. Chem.* **2008**, *1* (1), 601−626.

(12) Schlücker, S. Surface-Enhanced Raman Spectroscopy: Concepts and Chemical Applications. *Angew. Chem., Int. Ed.* **2014**, *53* (19), 4756−4795.

(13) Huck, C.; Neubrech, F.; Vogt, J.; Toma, A.; Gerbert, D.; Katzmann, J.; Härtling, T.; Pucci, A. Surface-Enhanced Infrared Spectroscopy Using Nanometer-Sized Gaps. *ACS Nano* **2014**, *8* (5), 4908−4914.

(14) Yockell-Lelièvre, H.; Lussier, F.; Masson, J.-F. Influence of the Particle Shape and Density of Self-Assembled Gold Nanoparticle Sensors on LSPR and SERS. *J. Phys. Chem. C* **2015**, *119* (51), 28577−28585.

(15) Wiley, B. J.; Chen, Y.; McLellan, J. M.; Xiong, Y.; Li, Z.-Y.; Ginger, D.; Xia, Y. Synthesis and Optical Properties of Silver Nanobars and Nanorice. *Nano Lett.* **2007**, *7* (4), 1032−1036.

(16) Adato, R.; Artar, A.; Erramilli, S.; Altug, H. Engineered Absorption Enhancement and Induced Transparency in Coupled Molecular and Plasmonic Resonator Systems. *Nano Lett.* **2013**, *13* (6), 2584−2591.

(17) Wu, C.; Khanikaev, A. B.; Adato, R.; Arju, N.; Yanik, A. A.; Altug, H.; Shvets, G. Fano-Resonant Asymmetric Metamaterials for Ultrasensitive Spectroscopy and Identification of Molecular Monolayers. *Nat. Mater.* **2011**, *11* (1), 69−75.

(18) Bukasov, R.; Shumaker-Parry, J. S. Silver Nanocrescents with Infrared Plasmonic Properties As Tunable Substrates for Surface Enhanced Infrared Absorption Spectroscopy. *Anal. Chem.* **2009**, *81* (11), 4531−4535.

DOI: 10.1021/acs.nanolett.7b00404
Nano Lett. XXXX, XXX, XXX−XXX

(19) Bühler, G.; Thölmann, D.; Feldmann, C. One-Pot Synthesis of Highly Conductive Indium Tin Oxide Nanocrystals. *Adv. Mater.* **2007**, *19* (17), 2224−2227.
(20) Kanehara, M.; Koike, H.; Yoshinaga, T.; Teranishi, T. Indium Tin Oxide Nanoparticles with Compositionally Tunable Surface Plasmon Resonance Frequencies in the Near-IR Region. *J. Am. Chem. Soc.* **2009**, *131* (49), 17736−17737.
(21) Wang, T.; Radovanovic, P. V. Free Electron Concentration in Colloidal Indium Tin Oxide Nanocrystals Determined by Their Size and Structure. *J. Phys. Chem. C* **2011**, *115* (2), 406−413.
(22) Garcia, G.; Buonsanti, R.; Llordes, A.; Runnerstrom, E. L.; Bergerud, A.; Milliron, D. J. Near-Infrared Spectrally Selective Plasmonic Electrochromic Thin Films. *Adv. Opt. Mater.* **2013**, *1* (3), 215−220.
(23) Zhu, Y.; Mendelsberg, R. J.; Zhu, J.; Han, J.; Anders, A. Structural, Optical, and Electrical Properties of Indium-Doped Cadmium Oxide Films Prepared by Pulsed Filtered Cathodic Arc Deposition. *J. Mater. Sci.* **2013**, *48* (10), 3789−3797.
(24) Gordon, T. R.; Paik, T.; Klein, D. R.; Naik, G. V.; Caglayan, H.; Boltasseva, A.; Murray, C. B. Shape-Dependent Plasmonic Response and Directed Self-Assembly in a New Semiconductor Building Block, Indium-Doped Cadmium Oxide (ICO). *Nano Lett.* **2013**, *13* (6), 2857−2863.
(25) Agrawal, A.; Kriegel, I.; Milliron, D. J. Shape-Dependent Field Enhancement and Plasmon Resonance of Oxide Nanocrystals. *J. Phys. Chem. C* **2015**, *119* (11), 6227−6238.
(26) Della Gaspera, E.; Chesman, A. S. R.; van Embden, J.; Jasieniak, J. J. Non-Injection Synthesis of Doped Zinc Oxide Plasmonic Nanocrystals. *ACS Nano* **2014**, *8* (9), 9154−9163.
(27) Buonsanti, R.; Llordes, A.; Aloni, S.; Helms, B. A.; Milliron, D. J. Tunable Infrared Absorption and Visible Transparency of Colloidal Aluminum-Doped Zinc Oxide Nanocrystals. *Nano Lett.* **2011**, *11* (11), 4706−4710.
(28) Mattox, T. M.; Bergerud, A.; Agrawal, A.; Milliron, D. J. Influence of Shape on the Surface Plasmon Resonance of Tungsten Bronze Nanocrystals. *Chem. Mater.* **2014**, *26* (5), 1779−1784.
(29) Kim, J.; Agrawal, A.; Krieg, F.; Bergerud, A.; Milliron, D. J. The Interplay of Shape and Crystalline Anisotropies in Plasmonic Semiconductor Nanocrystals. *Nano Lett.* **2016**, *16* (6), 3879−3884.
(30) Schimpf, A. M.; Lounis, S. D.; Runnerstrom, E. L.; Milliron, D. J.; Gamelin, D. R. Redox Chemistries and Plasmon Energies of Photodoped In_2O_3 and Sn-Doped In_2O_3 (ITO) Nanocrystals. *J. Am. Chem. Soc.* **2015**, *137* (1), 518−524.
(31) Schimpf, A. M.; Ochsenbein, S. T.; Buonsanti, R.; Milliron, D. J.; Gamelin, D. R. Comparison of Extra Electrons in Colloidal N-Type Al^{3+}-Doped and Photochemically Reduced ZnO Nanocrystals. *Chem. Commun.* **2012**, *48* (75), 9352−9354.
(32) Schimpf, A. M.; Knowles, K. E.; Carroll, G. M.; Gamelin, D. R. Electronic Doping and Redox-Potential Tuning in Colloidal Semiconductor Nanocrystals. *Acc. Chem. Res.* **2015**, *48* (7), 1929−1937.
(33) Garcia, G.; Buonsanti, R.; Runnerstrom, E. L.; Mendelsberg, R. J.; Llordes, A.; Anders, A.; Richardson, T. J.; Milliron, D. J. Dynamically Modulating the Surface Plasmon Resonance of Doped Semiconductor Nanocrystals. *Nano Lett.* **2011**, *11* (10), 4415−4420.
(34) Llordes, A.; Hammack, A. T.; Buonsanti, R.; Tangirala, R.; Aloni, S.; Helms, B. A.; Milliron, D. J. Polyoxometalates and Colloidal Nanocrystals as Building Blocks for Metal Oxide Nanocomposite Films. *J. Mater. Chem.* **2011**, *21* (31), 11631−11638.
(35) Kim, J.; Ong, G. K.; Wang, Y.; LeBlanc, G.; Williams, T. E.; Mattox, T. M.; Helms, B. A.; Milliron, D. J. Nanocomposite Architecture for Rapid, Spectrally-Selective Electrochromic Modulation of Solar Transmittance. *Nano Lett.* **2015**, *15* (8), 5574−5579.
(36) Adato, R.; Altug, H. In-Situ Ultra-Sensitive Infrared Absorption Spectroscopy of Biomolecule Interactions in Real Time with Plasmonic Nanoantennas. *Nat. Commun.* **2013**, *4*, 2154 DOI: 10.1038/ncomms3154.
(37) Adato, R.; Yanik, A. A.; Amsden, J. J.; Kaplan, D. L.; Omenetto, F. G.; Hong, M. K.; Erramilli, S.; Altug, H. Ultra-Sensitive Vibrational Spectroscopy of Protein Monolayers with Plasmonic Nanoantenna Arrays. *Proc. Natl. Acad. Sci. U. S. A.* **2009**, *106* (46), 19227−19232.
(38) Alici, K. B.; Gallardo, I. F. Detecting Secondary Structure and Surface Orientation of Helical Peptide Monolayers from Resonant Hybridization Signals. *Sci. Rep.* **2013**, *3*, 2956 DOI: 10.1038/srep02956.
(39) Runnerstrom, E. L.; Bergerud, A.; Agrawal, A.; Johns, R. W.; Dahlman, C. J.; Singh, A.; Selbach, S. M.; Milliron, D. J. Defect Engineering in Plasmonic Metal Oxide Nanocrystals. *Nano Lett.* **2016**, *16* (5), 3390−3398.
(40) Bhachu, D. S.; Scanlon, D. O.; Sankar, G.; Veal, T. D.; Egdell, R. G.; Cibin, G.; Dent, A. J.; Knapp, C. E.; Carmalt, C. J.; Parkin, I. P. Origin of High Mobility in Molybdenum-Doped Indium Oxide. *Chem. Mater.* **2015**, *27* (8), 2788−2796.
(41) Sachet, E.; Shelton, C. T.; Harris, J. S.; Gaddy, B. E.; Irving, D. L.; Curtarolo, S.; Donovan, B. F.; Hopkins, P. E.; Sharma, P. A.; Sharma, A. L.; Ihlefeld, J.; Franzen, S.; Maria, J.-P. Dysprosium-Doped Cadmium Oxide as a Gateway Material for Mid-Infrared Plasmonics. *Nat. Mater.* **2015**, *14* (4), 414−420.
(42) Chattopadhyay, D.; Queisser, H. J. Electron Scattering by Ionized Impurities in Semiconductors. *Rev. Mod. Phys.* **1981**, *53* (4), 745−768.
(43) Auguié, B.; Barnes, W. L. Collective Resonances in Gold Nanoparticle Arrays. *Phys. Rev. Lett.* **2008**, *101* (14), 143902 DOI: 10.1103/PhysRevLett.101.143902.
(44) Li, S.-Q.; Guo, P.; Buchholz, D. B.; Zhou, W.; Hua, Y.; Odom, T. W.; Ketterson, J. B.; Ocola, L. E.; Sakoda, K.; Chang, R. P. H. Plasmonic−Photonic Mode Coupling in Indium-Tin-Oxide Nanorod Arrays. *ACS Photonics* **2014**, *1* (3), 163−172.
(45) Urzhumov, Y. A.; Shvets, G.; Fan, J. A.; Capasso, F.; Brandl, D.; Nordlander, P. Plasmonic Nanoclusters: A Path towards Negative-Index Metafluids. *Opt. Express* **2007**, *15* (21), 14129.
(46) *Plasmonics: Fundamentals and Applications*; Springer US: Boston, MA, 2007.
(47) Lounis, S. D.; Runnerstrom, E. L.; Bergerud, A.; Nordlund, D.; Milliron, D. J. Influence of Dopant Distribution on the Plasmonic Properties of Indium Tin Oxide Nanocrystals. *J. Am. Chem. Soc.* **2014**, *136* (19), 7110−7116.
(48) Nicoletti, O.; de la Peña, F.; Leary, R. K.; Holland, D. J.; Ducati, C.; Midgley, P. A. Three-Dimensional Imaging of Localized Surface Plasmon Resonances of Metal Nanoparticles. *Nature* **2013**, *502* (7469), 80−84.
(49) Nelayah, J.; Kociak, M.; Stéphan, O.; García de Abajo, F. J.; Tencé, M.; Henrard, L.; Taverna, D.; Pastoriza-Santos, I.; Liz-Marzán, L. M.; Colliex, C. Mapping Surface Plasmons on a Single Metallic Nanoparticle. *Nat. Phys.* **2007**, *3* (5), 348−353.
(50) Kadkhodazadeh, S.; de Lasson, J. R.; Beleggia, M.; Kneipp, H.; Wagner, J. B.; Kneipp, K. Scaling of the Surface Plasmon Resonance in Gold and Silver Dimers Probed by EELS. *J. Phys. Chem. C* **2014**, *118* (10), 5478−5485.
(51) Barrow, S. J.; Collins, S. M.; Rossouw, D.; Funston, A. M.; Botton, G. A.; Midgley, P. A.; Mulvaney, P. Electron Energy Loss Spectroscopy Investigation into Symmetry in Gold Trimer and Tetramer Plasmonic Nanoparticle Structures. *ACS Nano* **2016**, *10* (9), 8552−8563.
(52) Leary, R. K.; Kumar, A.; Straney, P. J.; Collins, S. M.; Yazdi, S.; Dunin-Borkowski, R. E.; Midgley, P. A.; Millstone, J. E.; Ringe, E. Structural and Optical Properties of Discrete Dendritic Pt Nanoparticles on Colloidal Au Nanoprisms. *J. Phys. Chem. C* **2016**, *120* (37), 20843−20851.
(53) Yazdi, S.; Daniel, J. R.; Large, N.; Schatz, G. C.; Boudreau, D.; Ringe, E. Reversible Shape and Plasmon Tuning in Hollow AgAu Nanorods. *Nano Lett.* **2016**, *16* (11), 6939−6945.
(54) Ringe, E.; DeSantis, C. J.; Collins, S. M.; Duchamp, M.; Dunin-Borkowski, R. E.; Skrabalak, S. E.; Midgley, P. A. Resonances of Nanoparticles with Poor Plasmonic Metal Tips. *Sci. Rep.* **2015**, *5*, 17431.

DOI: 10.1021/acs.nanolett.7b00404
Nano Lett. XXXX, XXX, XXX−XXX

(55) Funston, A. M.; Novo, C.; Davis, T. J.; Mulvaney, P. Plasmon Coupling of Gold Nanorods at Short Distances and in Different Geometries. *Nano Lett.* **2009**, *9* (4), 1651−1658.
(56) Rechberger, W.; Hohenau, A.; Leitner, A.; Krenn, J. R.; Lamprecht, B.; Aussenegg, F. R. Optical Properties of Two Interacting Gold Nanoparticles. *Opt. Commun.* **2003**, *220* (1−3), 137−141.
(57) Kuznetsov, A. S. Effect of Proximity in Arrays of Plasmonic Nanoantennas on Hot Spots Density: Degenerate Semiconductors vs. Conventional Metals. *Plasmonics* **2016**, *11* (6), 1487−1493.
(58) Diaz-Egea, C.; Sigle, W.; van Aken, P. A.; Molina, S. I. High Spatial Resolution Mapping of Surface Plasmon Resonance Modes in Single and Aggregated Gold Nanoparticles Assembled on DNA Strands. *Nanoscale Res. Lett.* **2013**, *8* (1), 337.
(59) Hu, H.; Yang, X.; Zhai, F.; Hu, D.; Liu, R.; Liu, K.; Sun, Z.; Dai, Q. Far-Field Nanoscale Infrared Spectroscopy of Vibrational Fingerprints of Molecules with Graphene Plasmons. *Nat. Commun.* **2016**, *7*, 12334.
(60) Huck, C.; Vogt, J.; Sendner, M.; Hengstler, D.; Neubrech, F.; Pucci, A. Plasmonic Enhancement of Infrared Vibrational Signals: Nanoslits versus Nanorods. *ACS Photonics* **2015**, *2* (10), 1489−1497.
(61) Neubrech, F.; Beck, S.; Glaser, T.; Hentschel, M.; Giessen, H.; Pucci, A. Spatial Extent of Plasmonic Enhancement of Vibrational Signals in the Infrared. *ACS Nano* **2014**, *8* (6), 6250−6258.
(62) Fan, S.; Suh, W.; Joannopoulos, J. D. Temporal Coupled-Mode Theory for the Fano Resonance in Optical Resonators. *J. Opt. Soc. Am. A* **2003**, *20* (3), 569−572.
(63) Haus, H. A. *Waves and Fields in Optoelectronics*; Prentice Hall, Inc., 1984.
(64) Suh, W.; Wang, Z.; Fan, S. Temporal Coupled-Mode Theory and the Presence of Non-Orthogonal Modes in Lossless Multimode Cavities. *IEEE J. Quantum Electron.* **2004**, *40* (10), 1511−1518.

DOI: 10.1021/acs.nanolett.7b00404
Nano Lett. XXXX, XXX, XXX−XXX